Competing Channels for Hot-Electron Cooling in Graphene

Qiong Ma,[1] Nathaniel M. Gabor,[1] Trond I. Andersen,[1] Nityan L. Nair,[1] Kenji Watanabe,[2] Takashi Taniguchi,[2] and Pablo Jarillo-Herrero[1,*]

[1]Department of Physics, Massachusetts Institute of Technology, Cambridge, Massachusetts 02139, USA
[2]National Institute for Materials Science, Namiki 1-1, Tsukuba, Ibaraki 305-0044, Japan

(Received 21 March 2014; published 19 June 2014)

We report on temperature-dependent photocurrent measurements of high-quality dual-gated monolayer graphene *p-n* junction devices. A photothermoelectric effect governs the photocurrent response in our devices, allowing us to track the hot-electron temperature and probe hot-electron cooling channels over a wide temperature range (4 to 300 K). At high temperatures ($T > T^*$), we found that both the peak photocurrent and the hot spot size decreased with temperature, while at low temperatures ($T < T^*$), we found the opposite, namely that the peak photocurrent and the hot spot size increased with temperature. This nonmonotonic temperature dependence can be understood as resulting from the competition between two hot-electron cooling pathways: (a) (intrinsic) momentum-conserving normal collisions that dominates at low temperatures and (b) (extrinsic) disorder-assisted supercollisions that dominates at high temperatures. Gate control in our high-quality samples allows us to resolve the two processes in the same device for the first time. The peak temperature T^* depends on carrier density and disorder concentration, thus allowing for an unprecedented way of controlling graphene's photoresponse.

DOI: 10.1103/PhysRevLett.112.247401 PACS numbers: 78.67.Wj

Slow electron-lattice thermal equilibration is responsible for a plethora of new optoelectronic [1–4], transport [5,6], and thermoelectronic [7,8] phenomena in graphene. The wide temperature ranges (lattice temperature, 4 to 300 K) and long spatial scales in which hot carriers proliferate make graphene an ideal candidate for electronic energy transduction and numerous applications. Central to these are the unusual electron-phonon scattering pathways that dominate the cooling channels of graphene [7,9–13].

Unlike other materials, electron-lattice cooling at room temperature in graphene is dominated by an extrinsic three-body process [10]. This occurs when acoustic phonon emission is assisted by disorder scattering, called "supercollisions" (SC). SC dominates over the intrinsic momentum-conserving emission of acoustic phonons (normal collisions [NC]) for high temperatures. At low temperatures, the intrinsic process is expected to be dominant. However, the intrinsic NC process has never been experimentally observed before [11,14].

Here, we report on temperature-dependent spatially resolved photocurrent measurements of high-quality monolayer graphene (MLG) *p-n* junction devices. At the *p-n* interface, the photothermoelectric (PTE) effect dominates the photocurrent generation [2–4] and exhibits a nonmonotonic temperature dependence. We demonstrate that both the magnitude and spatial extent of the photoresponse are highly enhanced at an intermediate temperature T^*, indicating the coexistence of momentum-conserving NC cooling and disorder-assisted SC mechanisms. NC (SC) cooling dominates below (above) T^*, which can be tuned by varying the charge and impurity densities. In addition, we observed that the photoresponse at the graphene-metal (G-M) interface is also dominated by the PTE effect with a similar temperature-dependent behavior. Lastly, we show that the dramatic suppression of hot-carrier cooling at T^* allows for nonlocal control of hot-carrier dynamics. This involves top gate modulation of the photocurrent arising from illuminating the (distant) G-M interface.

Our MLG *p-n* junction devices are fabricated by micromechanical exfoliation, followed by standard electron-beam lithography techniques and thermal evaporation to define contacts (Cr/Au, 0.6/60 nm thick), as shown in Fig. 1(a). Hexagonal boron nitride flakes (10–20 nm thick) are then placed onto the samples as dielectric insulators by using a PMMA-transfer method, after which local top gates (Cr/Au, 0.6/100 nm thick) are fabricated to form *p-n* junctions in the center of the devices. In our experiments, the samples are kept in a liquid helium flow cryostat with an embedded resistive heater to give a precise temperature control from 4 K to above room temperature. We have measured eight SiO_2-supported exfoliated MLG devices with a high mobility of $\sim$10 000 cm^2/Vs, all of which show similar results. The data presented in this paper were collected from two of them: device 1 (8 μm long) and device 2 (6 μm long).

By tuning back gate (V_{BG}) and top gate (V_{TG}) voltages independently, the junction can be operated in four different charge configurations: *p-p*, *n-n*, *p-n* and *n-p* [3,4,15–17]. The photovoltage V_{PH} measured with a focused laser spot 1 μm in diameter (continuous wave, wavelength $\lambda = 850$ nm) fixed at the *p-n* interface as a function of V_{BG} and V_{TG} exhibits six regions of alternating signs [Fig. 1(b)], which has been shown to be the fingerprint of

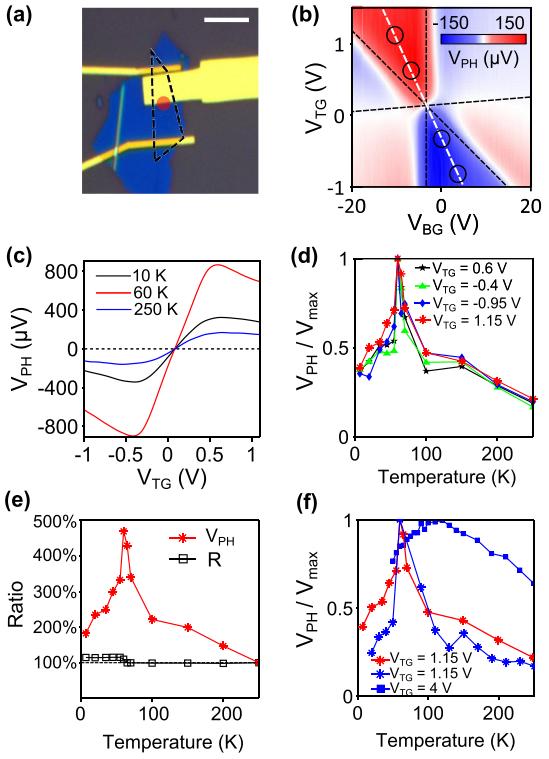

FIG. 1 (color online). (a) Optical microscope image of the device incorporating boron nitride top-gate dielectric. The dashed black line marks the boundary of graphene underneath the boron nitride. (b) Photovoltage V_{PH} versus V_{BG} and V_{TG} at $T = 250$ K with laser fixed at the p-n interface [red dot in (a)]. Optical power $P = 100$ μW. The white dashed line indicates $\mu_1 = -\mu_2$. (c) Traces of (b) for $\mu_1 = -\mu_2$ at different temperatures $T = 10$ K, $T = 60$ K, $T = 250$ K. Along $\mu_1 = -\mu_2$, the cooling profile is symmetric from the p-n interface. (d) V_{PH} as a function of temperature (normalized to the maximum value) at particular points [black circles in (b)] along the $\mu_1 = -\mu_2$ line. (e) Comparison between the temperature dependence of the photovoltage V_{PH} and the resistance R. Both V_{PH} and R are normalized by their values at $T = 250$ K. (f) The temperature dependence of V_{PH} at low ($|\mu_1| = |\mu_2| \approx 100$ MeV) and high ($|\mu_1| = |\mu_2| \approx 200$ MeV) densities, showing a shift of T^*. Red curve, device 1; blue curve, device 2.

the PTE effect [2–4]. This sixfold pattern is observed over a wide range of lattice (environment) temperatures from 4 up to 300 K. Figure 1(c) shows slices of the photovoltage plot for $\mu_1 = -\mu_2$ [dashed white line in Fig. 1(b)] at three representative temperatures (10, 60, and 250 K), where μ_1 and μ_2 are the chemical potentials in the single- and dual-gated regions, respectively. All three slices exhibit similar qualitative dependence on charge density, but the slice representing the intermediate temperature (60 K) is the greatest in magnitude, indicating a nonmonotonic dependence on temperature.

A detailed investigation of the relationship between photovoltage and lattice temperature is shown in Fig. 1(d), where V_{PH} is plotted as a function of temperature at four different points (circles) along the $\mu_1 = -\mu_2$ slice in Fig. 1(b), all of which exhibit a dramatic enhancement at $T^* = 60$ K. In comparison, only minor differences are observed for the measured resistance, R, within the same temperature range. We plot V_{PH} [same as the red line in Fig. 1(d)] and R (near the Dirac point) as a function of temperature in the same graph [Fig. 1(e)]. Both V_{PH} and R are normalized by their lowest values, which occur at $T = 250$ K. While V_{PH} shows an increase by as much as 500% at T^*, R stays fairly constant over the full temperature range (similar for R measured away from the Dirac point). In Fig. 1(f), we show the temperature dependence of V_{PH} collected from device 2 at low (blue star) and high (blue square) densities, both of which exhibit nonmonotonic behaviors but with an upwards shift of T^* from low to high density.

This nonmonotonic temperature dependence of the photoresponse is closely related to hot-electron dynamics in graphene. To illustrate this, we begin by describing the photovoltage as $V_{PH} = (S_1 - S_2)\Delta T_{pn}$ which determines the open-circuit PTE voltage generated from a sharply defined p-n junction [2,3] (ΔT_{pn} is the electronic temperature increase at the p-n interface). We assume a linear response regime where $T_e \gtrsim T_0$ [3] (T_0 is the lattice temperature) in the following analysis, which is consistent with the fact that all the measurements are performed in the linear power regime. By neglecting the temperature dependence of the resistance, $S_1 - S_2$ is linear in T [18,19], indicating a strong temperature dependence embedded in ΔT_{pn}.

With the laser focused on the p-n interface, a steady-state spatial profile of the electronic temperature T_e is established [Fig. 2(a) and 2(b)]. Material parameters that can affect the profile include the thermal conductivity κ, the electronic specific heat C_e, and the electron-lattice cooling rate γ. The combination of these three parameters generates a characteristic cooling length $\xi = (\kappa/\gamma C_e)^{1/2}$ for hot-carrier propagation in the system [2]. Due to the linear temperature dependence of both κ (Wiedemann-Franz law) and C_e, the temperature dependence of ξ is embedded in γ. The analytical solution to the heat equation of the system is $T_e(y) - T_0 = [\xi \sinh((\frac{1}{2}L - |y|)/\xi)/2\cosh(L/2\xi)](\dot{Q}/\kappa)$ (See Supplemental Material [20]), where $\dot{Q}$ is the rate at which heat enters the system and L is the device length (ΔT_{pn} is the value at $y = 0$). Figure 2(b) shows the spatial profile of $T_e - T_0$ in units of $\dot{Q}L/\kappa$, i.e., the dimensionless quantity $\xi \sinh((\frac{1}{2}L - |y|)/\xi)/2L\cosh(L/2\xi)$, for different values of ξ. The linear temperature dependence of S cancels out that of κ in the denominator of ΔT_{pn} when we multiply these to find the photoresponse V_{PH}. Consequently, the whole temperature dependence of V_{PH} is through ξ and thus ultimately via the cooling rate γ only. As can be seen from Fig. 2(c), the photoresponse, which is proportional to $\xi\sinh(L/2\xi)/2L\cosh(L/2\xi)$, grows quickly with ξ ($\gamma^{-(1/2)}$) and becomes saturated when ξ approaches the system length L.

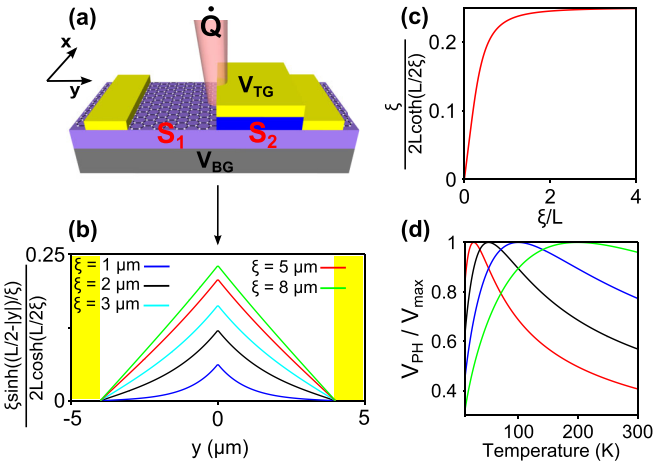

FIG. 2 (color online). (a) Schematic of a dual-gated graphene p-n junction device (global backgate V_{BG} and local topgate V_{TG}). $\dot{Q}$ denotes the rate at which heat enters the system by shining laser at the p-n interface. (b) Calculation of the quantity $\xi \sinh((\frac{1}{2}L - |y|)/\xi)/2L\cosh(L/2\xi)$, which is proportional to $T_e - T_0$, as a function of y for different cooling lengths. (c) Calculation of the quantity $\xi \sinh(L/2\xi)/2L\cosh(L/2\xi)$, which is proportional to the open-circuit photovoltage, as a function of ξ/L. ξ is the cooling length. L the device length. (d) Calculation of the temperature dependence of photovoltage generated with the laser fixed at the p-n interface with varying T_{BG} by using $k_{\mathrm{F}}\ell = 40$ (normalized to each peak). Red, $T_{\mathrm{BG}} = 6$ K; black, $T_{\mathrm{BG}} = 12$ K; blue, $T_{\mathrm{BG}} = 24$ K; and green, $T_{\mathrm{BG}} = 48$ K for chemical potential $\mu = 50, 100, 200, 400$ meV, respectively.

In order to understand the temperature dependence of γ, we consider possible hot-carrier cooling pathways in graphene. After initial relaxation of photoexcited carriers due to electron-electron scattering and optical phonon emission, the hot-carrier distribution cools by emitting acoustic phonons [9]. A relevant cooling process is single acoustic phonon emission with phase surface constraints (NC), which gives a slow cooling rate $\gamma_{\mathrm{NC}} = A/T$ with a prefactor A related to the charge density [9]. However, the disorder-assisted SC cooling gives rise to a competing cooling channel with a different cooling rate $\gamma_{\mathrm{SC}} = BT$, where the prefactor B is related to the amount of disorder and the charge density [10]. Therefore, NC and SC dominate at low and high temperatures respectively, with a cross-over temperature $T^* \approx (0.43\, k_{\mathrm{F}}\ell)^{1/2} T_{\mathrm{BG}}$ [10], where T_{BG} is the Bloch-Grüneisen temperature, k_{F} is the Fermi momentum, and ℓ is the disorder-dependent mean free path as modeled in Ref. [7,10,11,21]. The arguments above are valid under the condition $T \geq T_{\mathrm{BG}}$. At temperatures lower than T_{BG}, another regime of standard electron-phonon interaction without phase space constraints will play an important role [22,23]. T_{BG} is estimated from $k_{\mathrm{B}}T_{\mathrm{BG}} = \hbar s k_{\mathrm{F}}$ (s is the sound velocity in graphene) to be 12 K for the low density curves and 24 K for the high density curve in Fig. 1(f). Therefore, the nonmonotonic peaks observed in our measurements lie well in the range of $T \geq T_{\mathrm{BG}}$.

We see from the above that the optimal temperature for photodetection can be tuned by the disorder concentration (via $k_{\mathrm{F}}\ell$) and the charge carrier density (via T_{BG}), which can be understood in terms of the relative weight of NC and SC cooling pathways. The available phase space for NC cooling is expanded when increasing the charge carrier density, and the SC channel is suppressed by reducing the disorder concentration. Both changes result in an increase in the temperature range dominated by NC and a decrease in the range of SC behavior, which will cause T^* to increase. On the other hand, decreasing the carrier density and increasing the disorder amount will cause T^* to shift to lower temperatures. The shifting of T^* due to carrier density change is shown in Fig. 1(f) and Fig. 2(d) (simulation). To further verify the disorder relation, in-situ and systematic control of the disorder concentration is required. We want to emphasize that less disorder is always preferable in terms of the absolute efficiency of photocurrent at any temperatures.

The sensitivity of T^* to the charge density and disorder concentration may account for the different (monotonic) temperature-dependent behavior observed in previous studies [1,4,11,14,24–28]. In addition, all the above arguments are based on the $T_e \gtrsim T_0$ condition, while otherwise we need to consider the full expression of the relative cooling weight between the SC and NC, which is derived in Ref. [10] as $(0.77/k_{\mathrm{F}}\ell)(T_e^2 + T_e T_0 + T_0^2)/T_{\mathrm{BG}}^2$. The overheating of electrons ($T_e \gg T_0$) will strongly enhance the SC weight even at low lattice temperatures, completely masking the NC processes.

The NC-SC competition model describes well the nonmonotonic temperature dependence and the shifting of T^* as a function of the charge density. We note that substrate surface phonons may also contribute to hot-electron cooling, especially at higher temperatures [29–31], which could account for the discrepancies between the experimental data and the model (Supplemental Material, Fig. S3 [20]). Additionally, the enhancement observed near the peak temperature close to the charge neutrality point is much sharper and somewhat higher than the model predicts, which needs further investigation.

The nonmonotonic temperature dependence of hot-electron cooling is reflected not only in the magnitude of the photocurrent, but also in its spatial profile. Figure 3(a) shows the spatially resolved photocurrent microscopy ($V_{\mathrm{SD}} = 0$) of device 2. A strong photocurrent signal is observed at the p-n interface while the contact signals are strongly suppressed, which allows for independent extraction of the p-n signal profile. This signal decays with distance away from the p-n edge [denoted by a dashed black line in Fig. 3(a)] at different rates depending on temperature [Fig. 3(b)]. The lowest decay rate is observed at the peak temperature $T^* = 60$ K, corresponding to the longest cooling length.

We now turn to the G-M interface of device 1, where we also see evidence of a PTE response to laser illumination.

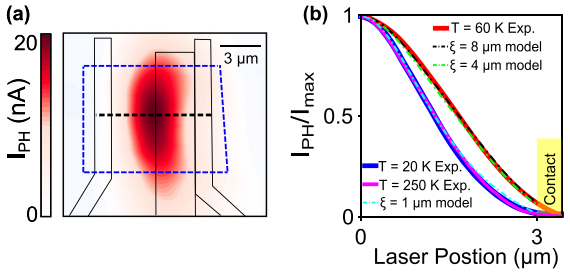

FIG. 3 (color online). (a) Spatially resolved photocurrent map at $T = 40$ K for device 2 ($V_{SD} = 0$ V, $V_{BG} = 25$ V, $V_{TG} = -2$ V). Solid black lines mark the location of gold contacts and top gate electrode. Dashed blue lines mark the boundaries of graphene. (b) Photocurrent line traces (normalized to the peak) taken along the dashed black line in (a) at different temperatures. Laser position = 0 corresponds to the edge of the top-gate electrode. Note: the photocurrent peaks have been symmetrized to remove small contact signals. For the simulation, we consider the convolution of the beam spot size 1 μm. More information about the simulation can be found in the Supplemental material [20].

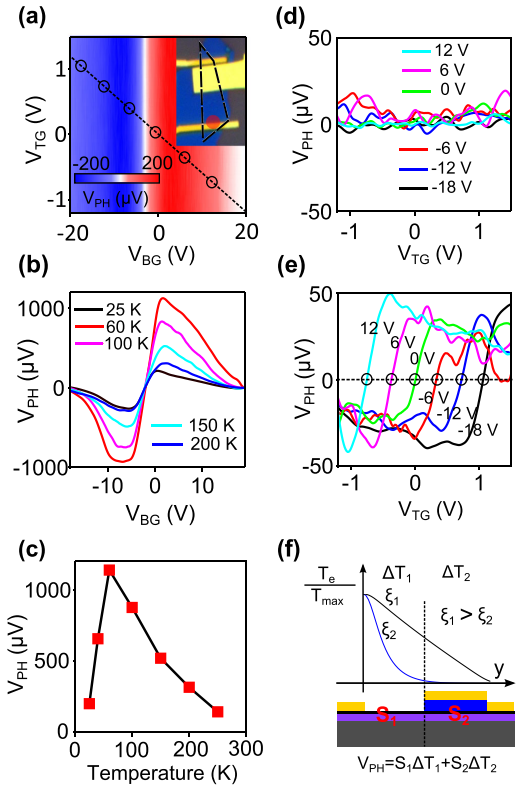

FIG. 4 (color online). (a) V_{PH} as a function of V_{BG} and V_{TG} with the laser fixed at the contact away from the top gate (ret dot in the inset figure) at $T = 250$ K. Along the dashed black line, the dual-gated region is charge neutral. Inset: optical image of the device marking the laser position as a red dot fixed at the contact away from the top gate electrode. (b) V_{PH} as a function of V_{BG} at a fixed top gate voltage $V_{TG} = 0.15$ V for different lattice temperatures. (c) The maximum V_{PH} in (b) as a function of the lattice temperature. (d) V_{PH} as a function of V_{TG} at fixed back gates [$T = 250$ K, vertical slices of (a)] exhibits no obvious top gate modulation. For each curve we have removed a constant background, i.e., the value along the diagonal dashed line in (a) (circles). (e) The same plot as in (d) for the peak temperature $T^* = 60$ K shows appreciable top gate modulation, which mimics the shape of the gate modulation of S_2. (f) Schematic of T_e as a function of the sample position y with the laser fixed at the left contact for both long and short cooling length scenarios. Note the different formula for V_{PH} because laser is now at one contact instead of at the p-n junction.

In order to avoid ambiguity, we fixed the laser at the interface away from the top gate electrode. Figure 4(a) shows the photovoltage V_{PH} as a function of V_{BG} and V_{TG} at 250 K, exhibiting complete reversal of polarity with respect to V_{BG}, which is consistent with previous studies [32–35]. Figure 4(b) plots V_{PH} slices as a function of V_{BG} (fixed V_{TG}) at various temperatures, showing once again that the photovoltage is maximized at an intermediate temperature (60 K) and thus has a nonmonotonic temperature dependence. The full temperature-dependent behavior of V_{PH} is shown in Fig. 4(c), where the maximum values of V_{PH} are plotted against temperature. We emphasize that this nonmonotonic temperature dependence due to the hot-electron cooling is unique to the PTE response and is not expected from the conventional photovoltaic (PV) effect, in which the separation of excited carriers by the built-in electric field leads to a net current [32–35]. Therefore, this serves as a strong indication that the PTE effect dominates the response to laser illumination of the G-M interface, consistent with recent reports where the photovoltaic contribution at 800 nm wavelength is relatively small [36].

Another important fact that can be extracted from Fig. 4(a) is that V_{PH} exhibits very little dependence on V_{TG} at $T = 250$ K. This is shown more clearly in Fig. 4(d), where V_{PH} is plotted as a function of V_{TG} at different back gate voltages [vertical slices of Fig. 4(a)]. Each curve has been subtracted by the value along the diagonal dashed line in Fig. 4(a), which defines the charge neutrality point of the dual-gated region. Indeed, no obvious top gate dependence is observable other than random fluctuations. In striking contrast, the same plot as Fig. 4(d), but at the peak temperature $T^* = 60$ K instead, exhibits clear top gate modulation [Fig. 4(e)], indicating nonlocal hot-carrier transport enhanced by a long cooling length.

This is further illustrated in Fig. 4(f). When the cooling length ξ is short either due to NC at low temperature or SC at high temperature, the hot carriers strongly thermalize with the lattice before reaching the top-gated region. This results in a low-temperature gradient ΔT_2 and thus a low PTE voltage in that region. Therefore, it is difficult to observe the modulation of S_2 by the top gate. In contrast, at the peak temperature T^*, the energy loss from the electronic system to the lattice is minimized. Hot carriers feature long

relaxation lifetimes and long spatial propagation, leading to a considerable ΔT_2 to drive S_2. In this regime, the top gate modulation is readily observable [Fig. 4(e)].

In conclusion, we have observed a strong nonmonotonic temperature-dependent behavior of the PTE response of high-quality graphene *p-n* and G-M junctions. This behavior originates from two competing mechanisms for hot-carrier cooling. At the peak temperature, hot carriers cool the slowest, resulting in a fivefold increase in the photocurrent generation with respect to room temperature and a dramatic nonlocal phenomenon. This optimal temperature for maximal hot-carrier extraction is controllable by carrier density and disorder concentration, which may pave the way for the design of more efficient graphene hot-carrier devices.

We thank J. C. W. Song and L. S. Levitov for numerous fruitful discussions. This work has been supported by AFOSR Grant No. FA9550-11-1-0225 (measurement and data analysis) and the Packard Fellowship program. Device fabrication was supported by a seed fund from S3TEC, an Energy Frontier Research Center funded by DOE, Office of Science, BES, under Grant No. DE-SC0001299/DE-FG02-09ER46577. This work made use of the Materials Research Science and Engineering Center Shared Experimental Facilities supported by the National Science Foundation (NSF) (Grant No. DMR-0819762) and of Harvard's Center for Nanoscale Systems, supported by the NSF (Grant No. ECS-0335765).

*pjarillo@mit.edu

[1] X. Xu, N. M. Gabor, J. S. Alden, A. M. van der Zande, and P. L. McEuen, Nano Lett. **10**, 562 (2010).
[2] J. C. W. Song, M. S. Rudner, C. M. Marcus, and L. S. Levitov, Nano Lett. **11**, 4688 (2011).
[3] N. M. Gabor, J. C. W. Song, Q. Ma, N. L. Nair, T. Taychatanapat, K. Watanabe, T. Taniguchi, L. S. Levitov, and P. Jarillo-Herrero, Science **334**, 648 (2011).
[4] D. Sun, G. Aivazian, A. M. Jones, J. S. Ross, W. Yao, D. Cobden, and X. Xu, Nat. Nanotechnol. **7**, 114 (2012).
[5] J. C. W. Song and L. S. Levitov, Phys. Rev. Lett. **109**, 236602 (2012).
[6] J. C. W. Song, D. A. Abanin, and L. S. Levitov, Nano Lett. **13**, 3631 (2013).
[7] A. C. Betz, S. H. Jhang, E. Pallecchi, R. Ferreira, G. Feve, J.-M. Berroir, and B. Placais, Nat. Phys. **9**, 109 (2013).
[8] S. Cho, S. D. Kang, W. Kim, E.-S. Lee, S.-J. Woo, K.-J. Kong, I. Kim, H.-D. Kim, T. Zhang, J. A. Stroscio *et al.*, Nat. Mater. **12**, 913 (2013).
[9] R. Bistritzer and A. H. MacDonald, Phys. Rev. Lett. **102**, 206410 (2009).
[10] J. C. W. Song, M. Y. Reizer, and L. S. Levitov, Phys. Rev. Lett. **109**, 106602 (2012).
[11] M. W. Graham, S.-F. Shi, D. C. Ralph, J. Park, and P. L. McEuen, Nat. Phys. **9**, 103 (2013).
[12] K. J. Tielrooij, J. C. W. Song, S. A. Jensen, A. Centeno, A. Pesquera, A. Zurutuza Elorza, M. Bonn, L. S. Levitov, and F. H. L. Koppens, Nat. Phys. **9**, 248 (2013).
[13] S.-F. Shi, T.-T. Tang, B. Zeng, L. Ju, Q. Zhou, A. Zettl, and F. Wang, Nano Lett. **14**, 1578 (2014).
[14] M. W. Graham, S.-F. Shi, Z. Wang, D. C. Ralph, J. Park, and P. L. McEuen, Nano Lett. **13**, 5497 (2013).
[15] J. R. Williams, L. DiCarlo, and C. M. Marcus, Science **317**, 638 (2007).
[16] B. Özyilmaz, P. Jarillo-Herrero, D. Efetov, D. A. Abanin, L. S. Levitov, and P. Kim, Phys. Rev. Lett. **99**, 166804 (2007).
[17] B. Huard, J. A. Sulpizio, N. Stander, K. Todd, B. Yang, and D. Goldhaber-Gordon, Phys. Rev. Lett. **98**, 236803 (2007).
[18] Y. M. Zuev, W. Chang, and P. Kim, Phys. Rev. Lett. **102**, 096807 (2009).
[19] P. Wei, W. Bao, Y. Pu, C. N. Lau, and J. Shi, Phys. Rev. Lett. **102**, 166808 (2009).
[20] See Supplemental Material at http://link.aps.org/supplemental/10.1103/PhysRevLett.112.247401 for details about transport characterization of devices, theoretical model and simulations, optical power dependence data and photocurrent profile at the contact.
[21] N. H. Shon and T. Ando, J. Phys. Soc. Jpn. **67**, 2421 (1998).
[22] S. S. Kubakaddi, Phys. Rev. B **79**, 075417 (2009).
[23] J. K. Viljas and T. T. Heikkilä, Phys. Rev. B **81**, 245404 (2010).
[24] J. M. Dawlaty, S. Shivaraman, M. Chandrashekhar, F. Rana, and M. G. Spencer, Appl. Phys. Lett. **92**, 042116 (2008).
[25] P. A. George, J. Strait, J. Dawlaty, S. Shivaraman, M. Chandrashekhar, F. Rana, and M. G. Spencer, Nano Lett. **8**, 4248 (2008).
[26] P. Plochocka, P. Kossacki, A. Golnik, T. Kazimierczuk, C. Berger, W. A. de Heer, and M. Potemski, Phys. Rev. B **80**, 245415 (2009).
[27] J. H. Strait, H. Wang, S. Shivaraman, V. Shields, M. Spencer, and F. Rana, Nano Lett. **11**, 4902 (2011).
[28] S. Winnerl, M. Orlita, P. Plochocka, P. Kossacki, M. Potemski, T. Winzer, E. Malic, A. Knorr, M. Sprinkle, C. Berger *et al.*, Phys. Rev. Lett. **107**, 237401 (2011).
[29] S. Fratini and F. Guinea, Phys. Rev. B **77**, 195415 (2008).
[30] M. Freitag, T. Low, and P. Avouris, Nano Lett. **13**, 1644 (2013).
[31] E. H. Hwang and S. Das Sarma, Phys. Rev. B **87**, 115432 (2013).
[32] E. J. H. Lee, K. Balasubramanian, R. T. Weitz, M. Burghard, and K. Kern, Nat. Nanotechnol. **3**, 486 (2008).
[33] J. Park, Y. H. Ahn, and C. Ruiz-Vargas, Nano Lett. **9**, 1742 (2009).
[34] T. Mueller, F. Xia, M. Freitag, J. Tsang, and P. Avouris, Phys. Rev. B **79**, 245430 (2009).
[35] F. Xia, T. Mueller, R. Golizadeh-Mojarad, M. Freitag, Y.-m. Lin, J. Tsang, V. Perebeinos, and P. Avouris, Nano Lett. **9**, 1039 (2009).
[36] T. J. Echtermeyer, P. S. Nene, M. Trushin, R. V. Gorbachev, A. L. Eiden, S. Milana, Z. Sun, J. Schliemann, E. Lidorikis, K. S. Novoselov *et al.*, arXiv:1402.1266.